Modeling the drying process of porous catalysts

Chemical Engineering Science 282 (2023) 119261

Contents lists available at ScienceDirect

Chemical Engineering Science

journal homepage: www.elsevier.com/locate/ces

Modeling the drying process of porous catalysts - impact of viscosity and surface tension

D.R. Rieder, E.A.J.F. Peters *, J.A.M. Kuipers

Multiphase Reactors Group, Department of Chemical Engineering and Chemistry, Eindhoven University of Technology, P.O. Box 513, 5600 MB Eindhoven, the Netherlands

ARTICLE INFO

Keywords:
Heterogeneous catalyst
Drying
Porous media
Non-linear properties

ABSTRACT

The distribution of catalytically active species in heterogeneous porous catalysts strongly influences their performance and durability within industrial reactors. A drying model for investigating this redistribution is developed and subsequently the impact of non-linear couplings of liquid viscosity and surface tension on hydrodynamics and redistribution of species during the drying process investigated. The gained insights are then used to exert control of the redistribution within the presented model by solely varying external process parameters.

1. Introduction

Heterogeneous catalysts are widely applied for the industrial production of chemicals, as their use often allows to conduct processes within realistic time scales, leads to economically favorable process conditions and can tune the selectivity towards certain products (Munnik et al., 2015). However, the most favorable catalytically active compounds often contain precious metals, which usually are a scarce resource and therefore an expensive, yet essential component. Additionally, the relevant deposits may be located in regions, where human rights and ecological welfare are not aligned with international standards (Mooiman et al., 2016). Therefore, maximizing the efficiency of the available material and thus reducing the required amount of those resources is crucial. As a common approach to intensify the use of the relevant compounds, those are often deposited on the surface of highly porous support materials. There, spreading within the pores leads to the maximization of contact area between reactants and catalyst.

Common type of reactors for the use of such supported catalysts are packed bed or fluidized bed reactors, where the supported catalyst is provided in the form of millimeter sized pellets. There, final performance of the target reactor is heavily dependent on the process parameters, the shape of the supported catalysts and the distribution of the catalytic compound within the porous material. Finding an optimal choice of the support structure is not always a trivial process, due to a variety of influences, i.e. pressure drop, intra- and inter-particle mass- and heat-transfer limitations or catalyst degradation to name a few (Jurtz et al., 2019). Among the various preparation possibilities for such structures, the incipient wetness approach is one of the most widely spread industrial processes. There, the support is first impregnated with a precursor solution, followed by a drying step and subsequent calcination (Munnik et al., 2015). All of those steps influence the final formation of the deposited catalyst from the atomic to the pellet level, thus posing an intricate and complex multiscale problem. Whereas the exact deposition mechanisms, form and dispersion of the final nanometer sized catalyst are not to be underestimated in their impact on the overall effectiveness, this work focuses on the redistribution phenomena within the porous pellet.

Early attempts to investigate the phenomena associated with the redistribution of species in catalyst pellets focused on the impregnation step (Maatman and Prater, 1957; Vincent and Merril, 1974), relying on post-drying profiles and under the assumption that fast drying minimizes movement of the contained species. Especially for precursor material with a strong adsorption on the target support, those approaches provided important insights into the relevant mechanisms. Currently, the interest in the impregnation step is still high, fueled by the ever improving experimental methods, e.g. highly resolved magnetic resonance imaging (Lysova et al., 2005; Bergwerff et al., 2007), UV-vis (van de Water et al., 2006) or Raman spectroscopy (Bergwerff et al., 2005). However, for industrially relevant precursor-support combinations and loads, the adsorptive forces often are not the dominating effect for the final distribution profile. There, the fluid movement induced by capillary-forces during the drying step is considered to dominate the

* Corresponding author.
E-mail address: e.a.j.f.peters@tue.nl (E.A.J.F. Peters).

https://doi.org/10.1016/j.ces.2023.119261
Received 9 May 2023; Received in revised form 24 August 2023; Accepted 5 September 2023
Available online 12 September 2023

Nomenclature

α	external heat transfer coefficient	W/m^2	
β	external mass transfer coefficient	m/s	
ϵ	volume fraction		
σ	surface tension	N/m	
σ_p	standard deviation of pore size distribution	m	
λ	thermal conductivity	W/(m K)	
μ	dynamic viscosity	Pa·s	
ρ	density	kg/m^3	
ζ	spatial variable		
ϕ	arbitrary variable		
θ	contact angle		
ω	mass fraction		
A	non-linear viscosity coefficient		
C	Gaussian normal distribution coefficient		
D	effective diffusion coefficient	m^2/s	
E	conservation error		
h	specific enthalpy	J/kg	
K	permeability	m^2	
k	partial permeability		
k_{prec}	precipitation reaction rate constant	kg/(m^3 s)	
S	saturation		
V	volume	m^3	
V_p	normalized pore volume		
$\mathbf{v}$	velocity	m/s	
c_p	isobaric heat capacity	J/(kg K)	
t	time	s	
J	flux	kg/(m^2 s)	
P	pressure	Pa	
P_∞	ambient pressure	Pa	
M	molar mass	mol/kg	
Y	load of precipitate	kg/kg	

intra-pellet mass transport and lead to a redistribution of the catalyst compound (Liu et al., 2010).

As the drying step attracted increasing interest by researchers, a variety of model approaches were investigated, of which the receding front model (Schlünder, 2004), as well as the volume averaged approach pioneered by Whitaker (1999) attracted significant attention. For a dedicated overview over popular drying models, the interested reader is referred to Vu and Tsotsas (2018). Initially developed and verified against macroporous materials, i.e. soil or wood (Perré and Turner, 1999), Whitaker's rigorously averaged formulation has also been successfully applied for the prediction of post-drying catalyst profiles in micro- and mesoporous materials (Liu et al., 2010; Lekhal et al., 2001; Noorithaya et al., 2019). However, those models incorporate a variety of phenomena, i.e. amphoteric supports, temperature and species dependent properties, formation of separated liquid pockets and evaporation. As those phenomena are all intrinsically linked, distinguishing the effect of each of them, as well as their interplay is a difficult task at best, if not outright impossible.

As a means to study the fundamental aspects of the drying of porous catalyst supports, a model is developed, based on the framework for drying in porous media by Vu and Tsotsas (2019). This model can then be used to understand the otherwise elusive transport phenomena associated with the redistribution of aqueous precipitating species within porous media. By increasing the complexity of the associated transport phenomena in a step-wise fashion, the relevance of the various aspects is then available for dedicated study.

Within this work, the characteristic strong dependence of the intra-pellet hydrodynamics on the exact coupling of the fluid properties to the process variables, such as temperature, pressure and concentration is investigated (Munnik et al., 2015; Liu et al., 2008; Börnhorst et al., 2016). Since the convective transport of the catalyst precursor is one of the main driving forces for redistribution during drying, it is of significant importance to understand the impact of those couplings, if the post-drying distribution of the catalyst within the porous support pellet should be controlled. Therefore, the interplay of temperature and species concentration on the viscosity, as well as the impact of varying capillary forces and varying drying temperature is investigated and discussed.

2. Modeling approach

2.1. Governing equations and boundary conditions

In this model, the four components water, air, aqueous species and precipitate, as well as heat transport are considered, as shown in Fig. 1.

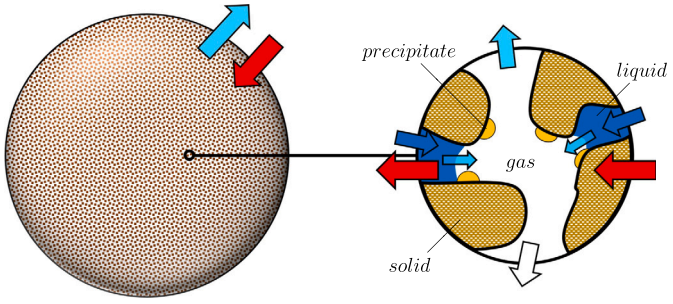

Fig. 1. Schematic overview of the drying model with the pellet (left) and the pore scale (right): On the pore scale, liquid (dark blue), water vapor (light blue), air (white) and energy transport (red) are considered, whereas the precipitate phase (yellow) is assumed to be immobile. Within the pores, evaporation occurs and capillary forces induce the transport of liquid. At the external boundary of the pellet, transport of water and heat is modeled, the gas phase is considered to be at ambient pressure at the boundary.

The conservation equation of water, air and energy is based on the numerical framework for flow in porous media described in detail by Vu and Tsotsas (2019) and extended with additional species transport and precipitation. The set of governing equations consists of the conservation equation of water w (1), air a (2), aqueous precipitating species (3), precipitate p (4) and the energy balance (5):

$$\frac{\partial}{\partial t}\left(\epsilon_l\rho_l\omega_{l,w}+\epsilon_g\rho_g\omega_{g,w}\right)+\nabla\cdot\left(\rho_l\omega_{l,w}\mathbf{v}_l+\rho_g\omega_{g,w}\mathbf{v}_g\right)=\nabla\cdot\left(\rho_g D_{g,av}\nabla\omega_{g,w}+\rho_l D_{l,wp}\nabla\omega_{l,w}\right) \tag{1}$$

$$\frac{\partial}{\partial t}\left(\rho_a\epsilon_g\right)+\nabla\cdot\left(\rho_a\mathbf{v}_g\right)=\nabla\cdot\left(\rho_g D_{g,av}\nabla\omega_{g,a}\right) \tag{2}$$

$$\frac{\partial}{\partial t}\left(\epsilon_l\rho_l\omega_{l,p}\right)+\nabla\cdot\left(\rho_l\omega_{l,p}\mathbf{v}_l\right)=\nabla\cdot\left(\rho_l D_{l,wp}\nabla\omega_{l,p}\right)-\epsilon_l r_{prec} \tag{3}$$

$$\frac{\partial}{\partial t}\left(\epsilon_s\rho_s\omega_{s,p}\right)=\epsilon_l r_{prec} \tag{4}$$

$$\begin{aligned}\frac{\partial}{\partial t}&\left(\epsilon_s\rho_s h_s+\epsilon_l\rho_l h_l+\epsilon_g\left(\rho_g\omega_{g,w}h_{g,w}+\rho_a h_{g,a}\right)\right)\\&+\nabla\cdot\left(\rho_l h_l\mathbf{v}_l+\left(\omega_{g,w}h_{g,w}+\rho_a h_{g,a}\right)\mathbf{v}_g\right)\\&=\nabla\cdot\left(\rho_g h_{g,a}D_{g,av}\nabla\omega_{g,a}\right)+\nabla\cdot\left(\rho_g h_{g,w}D_{g,av}\nabla\omega_{g,w}\right)\\&+\nabla\cdot\left(\rho_l h_l D_{l,wp}\nabla\omega_{l,w}+\rho_l h_l D_{l,wp}\nabla\omega_{l,p}\right)+\nabla\cdot\left(\lambda\nabla T\right)\end{aligned} \tag{5}$$

with the respective densities of liquid ρ_l and gas phase ρ_g, the volume fractions of solid, liquid and gas ϵ_s, ϵ_l and ϵ_g, the mass fractions of water, air, dissolved and precipitated species $\omega_{l,w}$, $\omega_{g,w}$, $\omega_{g,a}$, $\omega_{l,p}$ and $\omega_{s,p}$, as well as the enthalpy h_i of each component i. The porous solid media s is considered immobile and inert. Further, the effective binary diffusion

coefficients of the air-vapor and water-species are denoted as $D_{g,av}$ and $D_{l,wp}$. Here, the system is considered in thermal equilibrium with the representative temperature T. Thermal conduction is incorporated via an effective thermal conductivity λ. Convective transport is integrated via a Darcy-type of flow by the liquid and gas side velocity $\mathbf{v}_l$ and $\mathbf{v}_g$, explained in more detail below. Finally, the precipitation is modeled via an effective reaction rate r_{prec}. Note, that the precipitate is considered as immobile phase and pore-scale redistribution is neglected.
Precipitation is modeled in terms of the supersaturation $\omega^+_{l,p}$, with the associated tunable rate constant k_{prec}.

$$r_{prec} = k_{prec}\omega^+_{l,p} \tag{6}$$

$$\omega^+_{l,p} = \max(\omega_{l,p} - \omega_{l,p,sat}, 0) \tag{7}$$

For this model, it is assumed, that the outer boundary is exposed to a drying air stream at ambient temperature T_∞ with a representative value for the ambient water vapor pressure $P_{v,\infty}$. As the focus in this work is laid on a spherical geometry, no flux is acting there. Across the exposed surface water is only allowed to flow as vapor, allowing to define the boundary flux as:

$$\mathbf{J}_{g,w} \cdot \mathbf{n} = \beta P_\infty \frac{M_v}{RT} \ln\left(\frac{P_\infty - P_{v,\infty}}{P_\infty - P_v}\right) \tag{8}$$

with the external mass-transfer coefficient β, the ambient pressure P_∞, the ideal gas constant R and the molar weight of water M_v. For the energy equation, following boundary condition is applied:

$$\mathbf{J}_e \cdot \mathbf{n} = \alpha\left(T - T_\infty\right) + \Delta h_v J_w \tag{9}$$

with the external heat transfer coefficient α and the enthalpy of the vapor Δh_v. For the transport of air, the ambient pressure is prescribed at the outer boundary.

$$P_{g,bc} = P_\infty \tag{10}$$

Summing up all mass fractions in the liquid leads to unity:

$$\omega_{l,w} + \omega_{l,p} = 1 \tag{11}$$

Further, as the volume fraction of the precipitated species is considered negligible, a bootstrap can be formulated as

$$\epsilon_s + \epsilon_l + \epsilon_g = 1 \tag{12}$$

And thus the liquid saturation S_l can be expressed as:

$$S_l = \frac{\epsilon_l}{1 - \epsilon_s} \tag{13}$$

2.2. Fluid velocities and permeability model

The velocities of the gas and liquid phases are described by Darcy flow:

$$\mathbf{v}_l = -\frac{k_l K}{\mu_l}\nabla P_l \tag{14}$$

$$\mathbf{v}_g = -\frac{k_g K}{\mu_g}\nabla P_g \tag{15}$$

with the permeability of the porous medium K, the partial permeabilities of the liquid and gas phase k_l and k_g with their respective viscosities μ_l and μ_g, as well as the pressure gradients ∇P_l and ∇P_g. The pressures are correlated as follows:

$$P_g = P_a + P_v \tag{16}$$

$$P_l = P_g + P_c \tag{17}$$

with the capillary pressure P_c. Here it is assumed, that the ideal gas law is valid and therefore P_a and P_v are correlated to $\omega_{g,a}$ and $\omega_{g,w}$ via:

$$\frac{P_i}{\rho_g \omega_{g,i}} = \frac{1}{M_i} RT \tag{18}$$

with the molar mass M_i of species i. The capillary pressure is computed by the Young-Laplace law for a circular meniscus, assuming that the largest filled pore is dominating the pressure and the liquid shows a contact angle θ at the three-phase contact line with the surface tension σ:

$$P_c(r_p) = \frac{2\cos(\theta)\sigma}{r_p} \tag{19}$$

A very important characteristic of porous media is the total permeability K, as well as the partial permeabilities k_l and k_g as used in (14) and (15). To determine those permeabilities, they either can be acquired experimentally or derived analytically from routinely measured bulk properties (Metzger and Tsotsas, 2005; Yang et al., 2014; Miao et al., 2021; Thanh et al., 2023). Here, the approach by Metzger is adopted, where the bulk medium is approximated as a bundle of capillaries and subsequently the permeabilities and capillary pressure curves derived from pore size distributions (Metzger and Tsotsas, 2005). Note, that this approach overestimates the total permeability K by neglecting any tortuosity within the bulk medium. However, for this investigation the simplicity of the model outweighs its limitations.
Comparing Hagen-Poiseuille law with a bundle of capillaries leads to following relationship for the total permeability K:

$$K = \frac{1}{8}\int_{r_{p,min}}^{r_{p,max}} r_p^2 \frac{dV_p}{dr_p}\, dr_p \tag{20}$$

with the pore radius r_p of the distribution and its lower and upper limits $r_{p,min}$ and $r_{p,max}$, as well as the normalized volume distribution of the pores dV_p/dr_p. The partial permeabilities for liquid and gas phase can then be described as:

$$k_l = \frac{1}{8K}\int_{r_{p,min}}^{r_{p,f}} r_p^2 \frac{dV_p}{dr_p}\, dr_p \tag{21}$$

$$k_g = \frac{1}{8K}\int_{r_{p,f}}^{r_{p,max}} r_p^2 \frac{dV_p}{dr_p}\, dr_p \tag{22}$$

with the radius of the largest filled pore $r_{p,f}$. From (21) and (22) follows:

$$k_l + k_g = 1 \tag{23}$$

The largest filled pore can be found in dependence of the saturation of free liquid $S_{l,f}$ of the porous media:

$$S_{l,f} = \frac{S_l - S_{l,crit}}{1 - S_{l,crit}} = \frac{1}{1 - \epsilon_s}\int_{r_{p,min}}^{r_{p,f}} \frac{dV_p}{dr_p}\, dr_p \tag{24}$$

where $S_{l,crit}$ denotes the saturation content, at which a monolayer is adsorbed on the surface of the pores, convective flow stops and only evaporation is reducing the moisture, as described in section 2.3. Within this investigation, a monomodal pore size distribution in the form of a Gaussian normal distribution is considered:

$$\frac{dV_p}{dr_p} = \frac{C}{\sigma_p\sqrt{2\pi}} \exp\left(-\frac{1}{2}\left(\frac{r_p - r_{p,0}}{\sigma_p}\right)^2\right) \tag{25}$$

with the mean pore radius $r_{p,0}$, the standard deviation σ_p and the constant C, where $C \approx 1 - \epsilon_s$ for sufficiently large evaluation interval of the pore radii.

2.3. Treatment at low saturation

Once the critical saturation $S_{l,crit}$ is reached, where the fluid only exists adsorbed to the solid surface, convective fluid flow effectively

stops. From there on, solely evaporation and subsequent vapor transport leads to reduction of the remaining liquid. The evaporation process is modeled as an equilibrium phenomenon via the adsorption isotherm used by Perré and Turner (1999):

$$\phi = \begin{cases} \frac{S_l}{S_{l,crit}}\left(2 - \frac{S_l}{S_{l,crit}}\right) & \text{for } S \leq S_{l,crit} \\ 1 & \text{for } S_l > S_{l,crit} \end{cases} \tag{26}$$

with the saturation at the maximum amount of adsorbed water $S_{l,crit}$ and the relative humidity ϕ. Note, that for simplicity a dependency of the isotherm on r_p as follows from the Kelvin equation is neglected, further discussed in C.2. The partial permeabilities at $S_l < S_{l,crit}$ are given by:

$$k_l = 0 \tag{27}$$

$$k_g = 1 \tag{28}$$

2.4. Properties and couplings

For the determination of the effective diffusion coefficient of vapor in the gas phase, linear scaling with the area available for flux is assumed:

$$D_{g,av} = \epsilon_g D_{g,av,bin} \tag{29}$$

with the binary diffusion coefficient $D_{g,av,bin}$ of vapor in air. Similarly, $D_{l,wp}$ is formulated:

$$D_{l,wp} = S_{l,f}(1 - \epsilon_s) D_{l,wp,bin} \tag{30}$$

with the binary diffusion coefficient of the dissolved species in water $D_{l,wp,bin}$. The effective thermal conductivity is computed as arithmetic average quantity and by neglecting conduction in the gas phase:

$$\lambda = \epsilon_s \lambda_s + \epsilon_l \lambda_l \tag{31}$$

The enthalpy of all the solid, water, precipitate and air is computed by:

$$h_i = c_{p,i}(T - T_{ref}) \tag{32}$$

where T_{ref} denotes a reference temperature and $c_{p,i}$ the relevant heat capacity. For the vapor phase, the evaporation enthalpy Δh_v is additionally taken into account:

$$h_{g,w} = c_{p,v}(T - T_{ref}) + \Delta h_v \tag{33}$$

2.5. Numerical details

For numerically solving the set of non-linear partial differential equations, a finite-volume approach for the discretization was chosen and Newton-Raphson iterations were employed within a Mathworks® MATLAB implementation. The associated Jacobian is determined via numerical differentiation of the defect with a step size of 10^{-10} relative to the field value. For the species transport, a MINMOD TVD scheme was applied to the convective fluxes.

Especially during early timesteps, the model may predict strong gradients of the liquid saturation S_l, leading to a 'drying front'. This sharp change in parameters may induce numerical oscillations, if the gradient is insufficiently resolved. To alleviate this issue, the grid spacing is reduced along the dimensionless spacial variable ζ towards the drying surface:

$$\zeta = r/R \tag{34}$$

$$\Delta\zeta(n) = \frac{(1 + \Delta\zeta_{min}) - \zeta(n)}{\sum_n^{n_{tot}}(1 + \Delta\zeta_{min}) - \zeta(n)} \tag{35}$$

with the grid cell number n and minimal relative grid spacing $\Delta\zeta_{min}$ at $\zeta \longrightarrow 1$. For this investigation, a grid resolution of $n_{tot} = 100$ cells and $\Delta\zeta_{min} = 0.01$ were considered sufficient. Further details can be found in Appendix B.

3. Results

As model porous support, a sphere was chosen with a radius of $R_s = 2$ mm and a solid volume fraction of $\epsilon_s = 0.4$. For the pore size distribution within the support, the mean diameter $d_{p,0} = 10$ nm with a standard deviation of $\sigma_p = 2$ nm were used in (25). The distribution was evaluated within the range of 5 - 15 nm. For the critical saturation, a value of $S_{l,crit} = 0.35$ was assumed and for the mass transport, an initial concentration on $c_0 = 0.1 c_{sat}$ was employed. Further details can be found in Appendix C.

As the goal of this study is to understand the influence of the coupling of the relevant macroscopic properties on species redistribution, the focus is laid on the couplings which influence the liquid velocity in (14). As a first step, the focus is laid on the viscosity due to its commonly complex interaction with temperature and species concentration. In a second step, the dependence on the capillary forces induced by the capillary pressure (19) is investigated by means of an effective surface tension.

To study the impact of the coupling of transport parameters with species and temperature, viscosity and effective surface tension were investigated at the three drying temperatures $T_\infty = 20$, 100 and 200 °C. In all cases, the ambient water vapor pressure was set to $P_{v,\infty} = 0$ Pa. The drying is considered complete, once saturation at any point within the sphere does not exceed 10^{-6}.

For convenience, the precipitated species is expressed in terms of load on the solid porous material:

$$Y = \frac{\omega_{s,p}\epsilon_s\rho_s}{(\epsilon_s\rho_s)_0} \tag{36}$$

with the initial mass of the unloaded support $(\epsilon_s\rho_s)_0$. Additionally, as this work focuses on the interplay of species transport with viscous and capillary forces, it is pertinent to introduce the capillary number Ca and the Peclet number Pe for characterization of the transport phenomena:

$$Ca = \frac{\mu_l \mathbf{v}_l}{\sigma} \tag{37}$$

$$Pe = \frac{R_s \mathbf{v}_l}{D_{l,wp}} \tag{38}$$

3.1. Viscosity

As a means to study the impact of liquid viscosity, three formulations for the viscosity coupling were investigated:

$$\mu_{l,I} = const. \tag{39}$$

$$\mu_{l,II} = \mu_{l,0} + \frac{\omega_{l,p}}{\omega_{sat}}(\mu_{sat} - \mu_{l,0}) \tag{40}$$

$$\mu_{l,III} = 1.19 \cdot 10^{-6} \exp\left(A\frac{\omega_{l,p}}{\omega_{sat}} + A^2\frac{\omega_{l,p}^2}{\omega_{sat}^2}\right) T^{\frac{1}{2}} \exp\left(\frac{600\ \text{K}}{T - 139\ \text{K}}\right) \frac{\text{Pa}\cdot\text{s}}{\text{K}^{\frac{1}{2}}} \tag{41}$$

Note, that $\mu_{l,III}$ adopts a combination of an isothermal exponential term and the Vogel-Fulcher-Tamman formula for non-isothermal viscosity, both described in (Mahiuddin and Ismail, 1996). The range of the investigated viscosity values was set to $0.001 \leq \mu_l \leq 1$ Pa · s. For pure water, a viscosity of $\mu_{l,0} = 0.001$ Pa · s was used, whereas commonly used catalyst precursors can exhibit values of $\mu_l \approx 2 - 30$ Pa · s (Abdulagatov et al., 2006; Bentaleb et al., 2014), higher values of approximately $\mu_l = 1$ Pa · s can easily be reached, e.g. with glycerol-water mixtures (Segur and Oberstar, 1951).

By manipulating the factor A in (41), the viscosity at saturation can be adjusted, as shown in Fig. 2a. An example for the dependency on the temperature T at various weight fractions $\omega_{l,p}$ is provided for $\mu_{sat} = 1$ Pa · s in Fig. 2b.

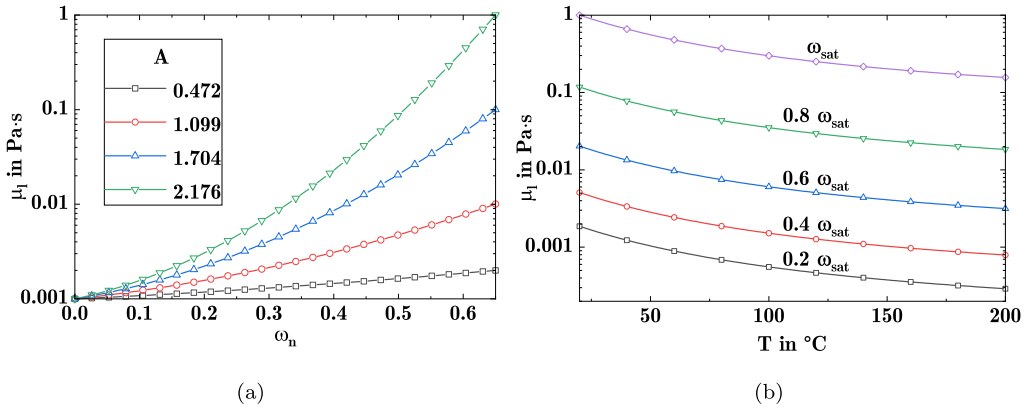

Fig. 2. Non-linear viscosity for (a) varying values of A with $\mu_{l,0} = 0.001$ Pa · s and μ_{sat} in the range of 0.002 - 1 Pa · s at $T = 20$ °C and (b) varying T and $\omega_{l,p}$ for $\mu_{sat} = 1$ Pa · s.

In Fig. 3a, the load distributions of the precipitate are displayed for several values of the constant viscosity $\mu_{l,I}$ following drying at $T_\infty = 100$ °C. There, a clear shift is visible from preferred precipitation at the surface of the sphere at $r = 2$ mm for low viscosity to an accumulation of precipitate at the center at $r = 0$ mm for high viscosity. Additionally, for highly viscous liquids ($\mu_{l,I} > 0.2$ Pa · s), a maximum load slightly off center can the observed. Further, the saturation and weight fraction profiles at the average concentration $S_{l,avg} = 0.35$ are depicted in Fig. 3c, highlighting the development of more pronounced profiles at higher liquid viscosity, higher concentration at the center for higher viscosity values and rise of the weight fraction towards precipitation levels for low values of S_l. The maximum instantaneous Ca was found to range between $Ca = 1.2 \cdot 10^{-8}$ for $\mu_{l,I} = 0.002$ Pa · s and $Ca = 3.4 \cdot 10^{-6}$ for $\mu_{l,I} = 1$ Pa · s. At the same time, the maximum value of Pe amounts to $Pe = 0.51$ for $\mu_{l,I} = 0.002$ Pa · s and decreases to $Pe = 0.29$ for $\mu_{l,I} = 1$ Pa · s. In Fig. 3d the progression of the saturation profile over time in the case of $\mu_l = 1$ Pa · s in Fig. 3d is provided.

An example for the profiles of the internal gas pressure P_g and the complementary liquid saturation profiles S_l inside the particle is provided in Fig. 4. There it is visible, that maximum of P_g increases over time and the profile exhibits two distinctive sections: The first section is characterized by almost constant pressure in the center region of the particle, whereas the second section shows a gradual decrease in P_g towards the ambient pressure P_∞ at the drying surface. Further the contact points between those two sections coincide with the point where S_l reaches the critical saturation $S_{l,crit}$. In the case of the first and last shown timestep, no significant build up of P_g could be observed. In order to understand the shift in the precipitate profile with increasing liquid viscosity it is pertinent to first focus on the associated changes in the instantaneous saturation and weight fraction profiles in Fig. 3c. There the increase of Ca with μ_l and thus a higher impact of the viscous forces then leads to a reduced capillary suction towards the surface and require evaporation to take place inside the porous object. As a result, a strong gradient in the saturation profile is induced, leading to the formation of a 'drying front' for higher viscosity values. The development of such saturation profiles as well as their dependency on the viscosity of the fluid medium is in accordance with earlier findings based on pore network models (Prat and Bouleux, 1999; Kharaghani et al., 2021). This is also directly correlated to the drying rate curves in Fig. 3b, where the reduced viscous forces allow to sustain the convective liquid flow to the surface for an extended period of time and subsequently to longer constant drying rate periods. A side effect thereof is also the overall decrease of the overall drying time for lower viscosity.

Due to the reduction of the local liquid saturation, the weight fraction of species increases, thus inducing a driving force for the diffusive flux towards the center of the pellet and leading to simultaneously higher liquid saturation and weight fraction levels. This insight then allows to understand the shift in precipitation profile in Fig. 3a. The convective fluxes lead to transport of species towards the surface and evaporation increases the local mass fraction $\omega_{l,p}$. As a result, a gradient in the mass fraction is introduced that serves as driving force for the diffusive fluxes towards the center of the sphere. In the case of low liquid viscosity values, the comparatively high Pe accommodates the strong accumulation at the surface. In contrast, with increasing viscosity values, Pe decreases and the diffusive fluxes lead to preferred accumulation at the center. The shifted maximum load at higher liquid viscosity is caused by the competition of the induced diffusive flux with the evaporation rate. On the one hand, the concentration gradient decreases in the later drying stage due to the aforementioned accumulation in the center, reducing the driving force for the diffusive flux. On the other hand, the heat flux is counteracted by evaporation leading to the formation of the aforementioned 'drying front', as visible in Fig. 3d. This drying front develops with increasing speed towards the center and finally leads to precipitation of the still aqueous species in the apparent profile.

As for the gas pressure profiles in Fig. 4, they are induced by the presence of the receding drying front. As soon as the S_l falls below the critical value, the local moisture is reduced by evaporation, which leads to a local rise in pressure and subsequently induced vapor transport towards the surface. With increasing distance of the drying front to the pellet surface, a higher gas pressure is formed to accommodate the transport of the continuously evaporating liquid along the pressure gradient. During the constant drying rate regime early on in the drying process, when the surface of the pellet is wet, e.g. at $t = 200$ s, no significant increase in gas pressure drop occurs. Similarly, once the pellet has reached a comparatively dry state at the end of the drying process and the evaporation rate is significantly reduced, e.g. at $t = 1200$ s, the gas pressure equilibrates to ambient conditions.

The impact of the viscosity couplings $\mu_{l,II}$ and $\mu_{l,III}$ under the same drying conditions is shown with examples at $\mu_{sat} = 0.002$ Pa · s and $\mu_{sat} = 0.1$ Pa · s in Fig. 5. For the case, where the liquid viscosity at saturation is low, no distinctive differences in the precipitate profile can be observed. In contrast, for higher saturation viscosity, a distinctive change in profile can be observed. Both profiles are caused by the level of the liquid viscosity throughout the domain. For $\mu_{sat} = 0.002$ Pa · s the viscosity always is within the same order of magnitude, independent of the local concentration, thus leading only to marginal changes in the local convective flow and subsequently almost identical profiles. However, for higher μ_{sat}, the convective flow is highly dependent on the interplay of species transport with viscosity and vice versa. There the liquid viscosity for the coupled formulations throughout the drying is significantly lower than μ_{sat} as shown in Fig. 5c, allowing for higher convective liquid flow rates towards the surface. This also leads to the significantly different saturation profiles at $S_{l,avg} = 0.5$, visible in 5d. In the case of constant viscosity $\mu_{l,I}$ a pronounced saturation profile can be observed, whereas the linear coupling $\mu_{l,II}$ induces a less severe saturation gradient and the non-linear coupling $\mu_{l,III}$ shows

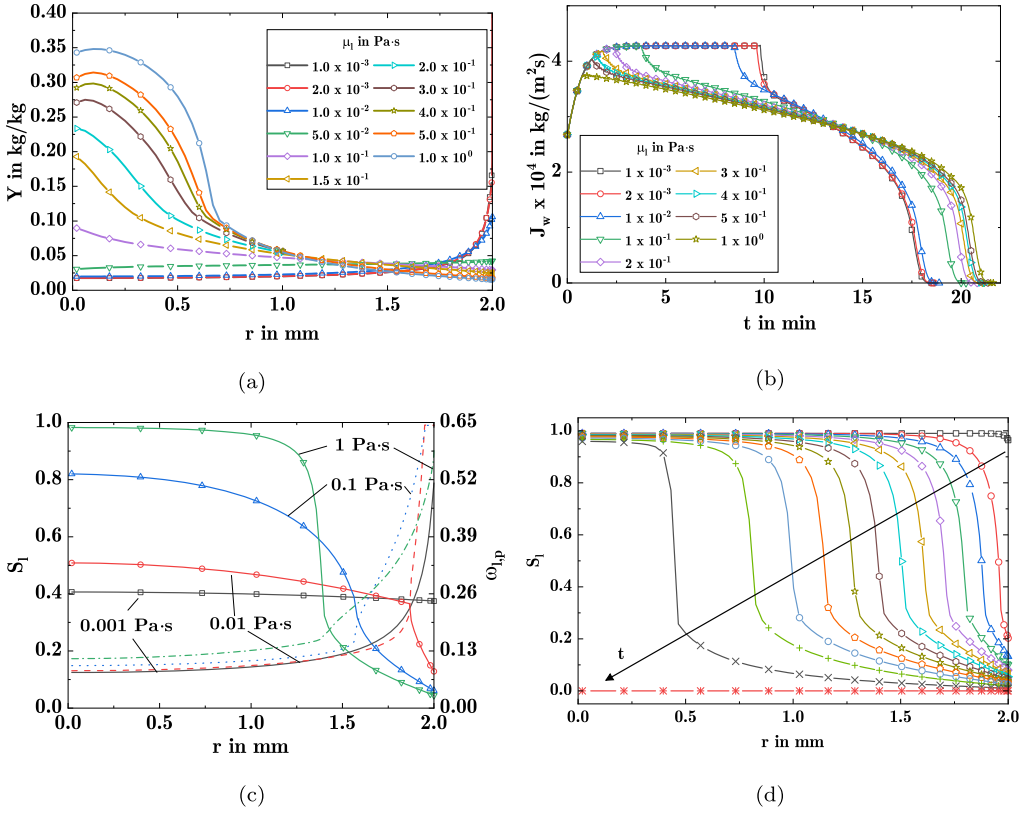

Fig. 3. Results for drying at $T_\infty = 100\,^\circ\text{C}$ and several values of constant viscosity: (a) precipitate load distribution, (b) vapor flux at the surface, (c) saturation and species weight fraction profiles at $S_{l,avg} \approx 0.35$ (scatter-line for S_l, dashed line for $\omega_{l,p}$) and (d) development of saturation profiles over time at time intervals $\Delta t = 100$ s with a viscosity of 1 Pa · s. *Note: the provided symbols serve visibility and are only loosely correlated with the actual numerical grid.*

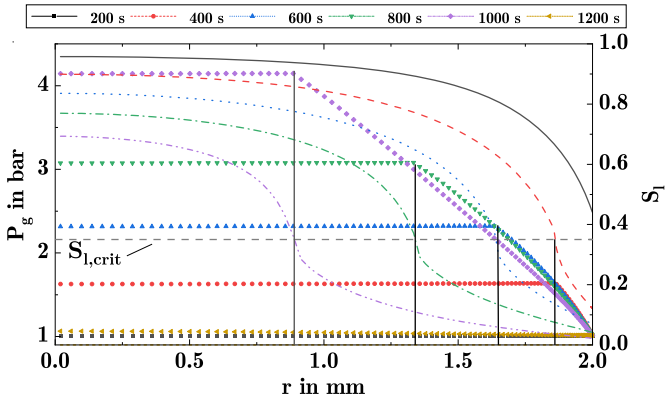

Fig. 4. Gas pressure (dots) and saturation profiles (lines) at various timesteps for $\mu_{l,I} = 0.1$ Pa · s and $T_\infty = 100\,^\circ\text{C}$. The black vertical lines are provided as indicator for the localization of $S_{l,crit}$ in the separate saturation profiles.

an almost uniform saturation profile. It is noteworthy, how the values of $\mu_{l,III}$ in Fig. 5c throughout the domain remain far below the viscosity at saturation and therefore promote a saturation curve and drying behavior similar to the cases of constant viscosity in the range of $0.002\ \text{Pa} \cdot \text{s} < \mu_{l,I} < 0.01\ \text{Pa} \cdot \text{s}$ in Fig. 3. The coupling between the viscosity and the species transport also leads to observable changes in drying behavior on the pellet-level, as shown in Fig. 6 in terms of the external vapor flux J_w. Evidently, the constant drying rate period is prolonged for $\mu_{l,III}$ and $\mu_{l,II}$, as the capillary forces continue to dominate the liquid transport for an extended period of time and viscous forces gain importance only later in the drying process, as the species accumulates at the drying front. Further upholding the constant drying rate period then also leads to a slight decrease in total drying time for $\mu_{l,III}$ decreases in contrast to $\mu_{l,II}$ and a more significant reduction compared with $\mu_{l,I}$.

3.2. Surface tension and contact angle

Within this model, the surface tension σ and the contact angle θ are inseparably linked, as shown in (19). Therefore, their impact is studied by introducing a manipulated surface tension σ^*, which is then varied:

$$\sigma^* = \cos(\theta)\sigma \tag{42}$$

To simplify the notation, the superscript will be dropped and σ employed to describe the effective surface tension. For studying the impact of the capillary forces, two formulations for the effective surface tension σ_{eff} were investigated:

$$\sigma_{eff,I} = const. \tag{43}$$

$$\sigma_{eff,II} = \exp(\omega_{l,w}\ln(\sigma_w) + (1-\omega_{l,w})\ln(\sigma_p)) \tag{44}$$

where σ_p in (44) denotes the surface tension of the (hypothetical) molten salt as described in (Dutcher et al., 2010). For the surface tension of water, a value of $\sigma_w = 0.072$ N/m is assumed. In this investigation, σ_p is varied between 0.038-0.108 N/m. As a first step, $\sigma_{eff,I}$ was varied while the viscosity was kept constant at $\mu_{l,I} = 100$ Pa · s to study the impact of the effective surface tension, shown in Fig. 7a. There, a decrease of $\sigma_{eff,I}$ leads to a more pronounced shift of the load to the center of the sphere, whereas an increase of $\sigma_{eff,I}$ induces a more homogeneous spread. This effect can be explained by the change in viscous to capillary forces represented by Ca. For lower σ and subsequently higher Ca, the viscous forces lead to a more pronounced drying front, as described above, whereas higher σ has the opposite effect.

In a second step, a more realistic system is investigated by combining the species dependent $\sigma_{eff,II}$ with $\mu_{l,III}$ that has a non-linear de-

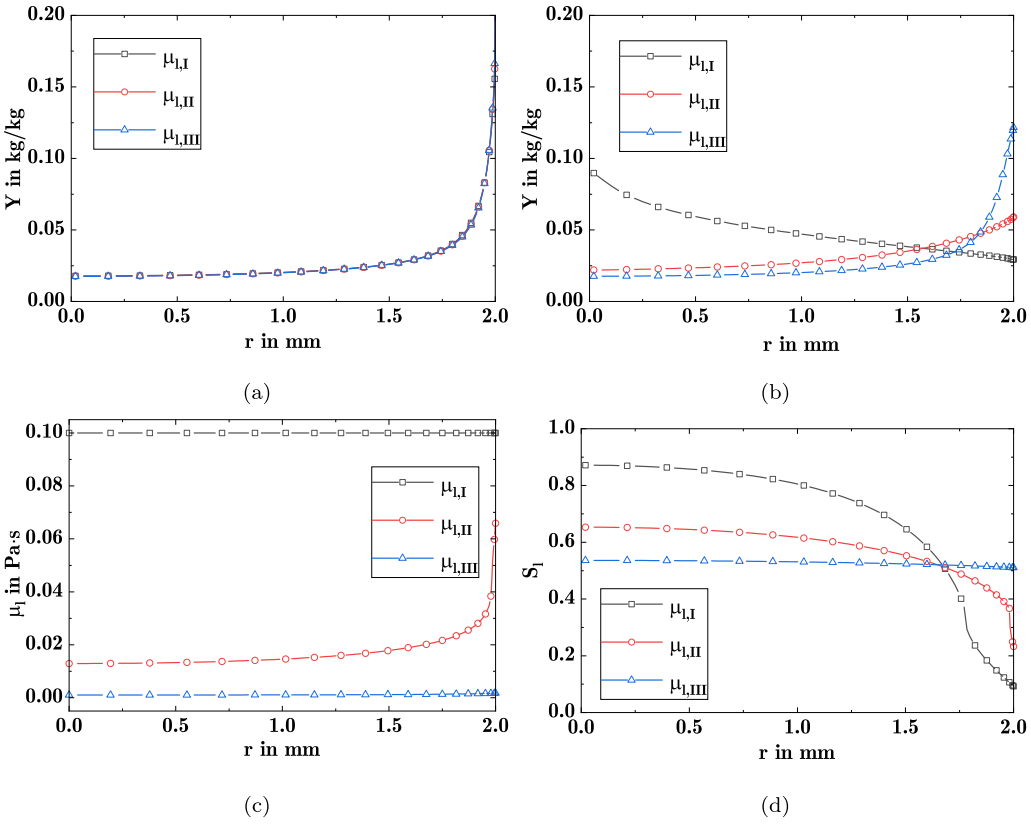

Fig. 5. Results for drying with varying viscosity types: post-drying precipitate distribution at (a) 2 m Pa · s and (b) 0.1 Pa · s, as well as profiles with $\mu_{sat} = 0.1$ Pa · s and varying (c) μ_l and (d) S at $S_{l,avg} = 0.5$.

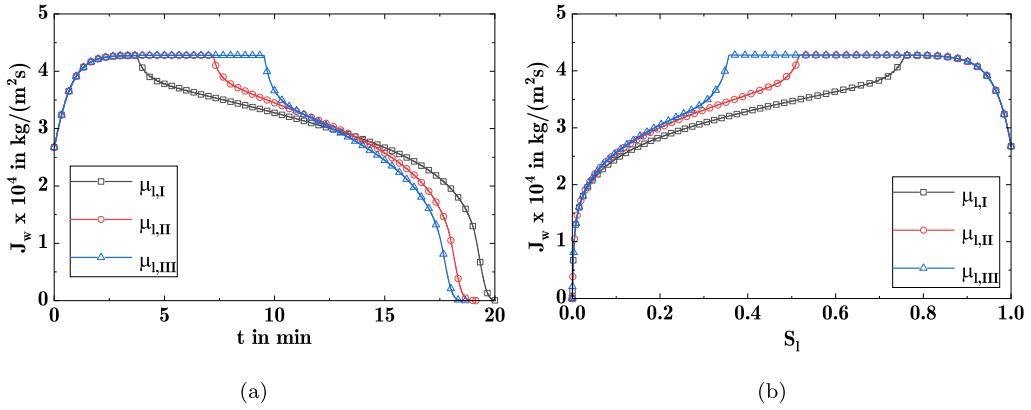

Fig. 6. Water vapor flux during the drying at $T_\infty = 100\,°C$ for varying viscosity types with a maximum viscosity of 100 m Pa · s (a) over time and (b) over saturation.

pendency on the weight fraction of the precipitating species and the resulting precipitate distribution is displayed in Fig. 7b. Seemingly, the species dependent surface tension has a negligible effect on the overall precipitate load profile, with only a marginal tendency to a more pronounced profile for higher σ_p. Continuing on the reasoning above this comes as no surprise, as the viscosity for the majority of the drying process is low enough to reduce $Ca < 2 \cdot 10^{-8}$ even for $\sigma_p = 0.036$ N/m. Subsequently, convective flux stays relevant for the species transport and induces accumulation at the pellet surface, as indicated by $Pe \approx 0.5$.

3.3. Drying temperature

Lastly, the impact of different drying temperatures on the drying behavior and the final distribution of the precipitate load was investigated. Here, the non-linear formulation for the liquid viscosity in (41) was employed, while for the surface tension the constant formulation $\sigma_{eff,I} = 0.072$ N/m was chosen. The results are laid out in Fig. 8.

As shown in Fig. 8a, higher drying temperatures induce a more pronounced shift of the load distribution towards the surface of the sphere, whereas a lower drying temperature lead to a more uniform distribution. The reason therefore can be found in: 1) the higher drying rate at higher T_∞ seen in Fig. 8b leads to a higher convective flux towards the surface, favoring the accumulation close to the surface, 2) the higher drying rate is supported by the temperature-induced lower viscosity in of the liquid as seen in Fig. 8c, allowing to sustain the higher evaporation rate close to the surface and 3) the overall reduced time required for drying also reduces the amount of backwards-diffusion of the species towards center of the sphere, allowing for less equilibration of the species concentration. Another observation is the change of onset of the falling drying rate period at larger averaged saturation for higher

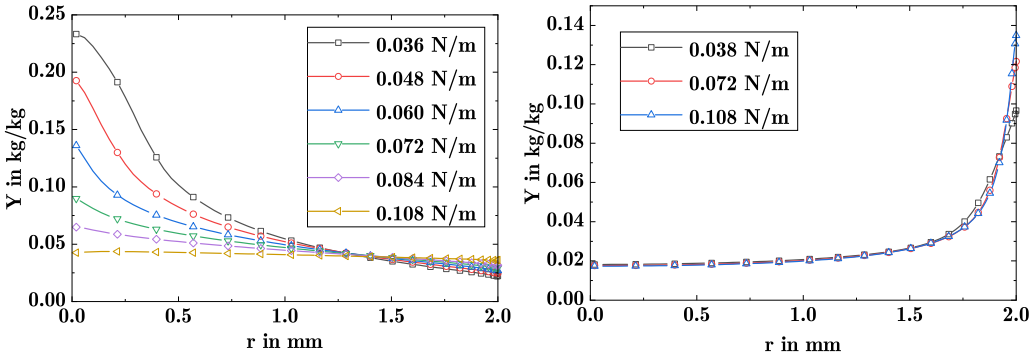

Fig. 7. Precipitate distribution for drying at $T_\infty = 100\,^\circ$C with (a) varying $\sigma_{eff,I}$ at $\mu_{l,I} = 0.1$ Pa · s and (b) varying σ_p combined with $\mu_{l,III}$ with a saturation viscosity of $\mu_{sat} = 0.1$ Pa · s.

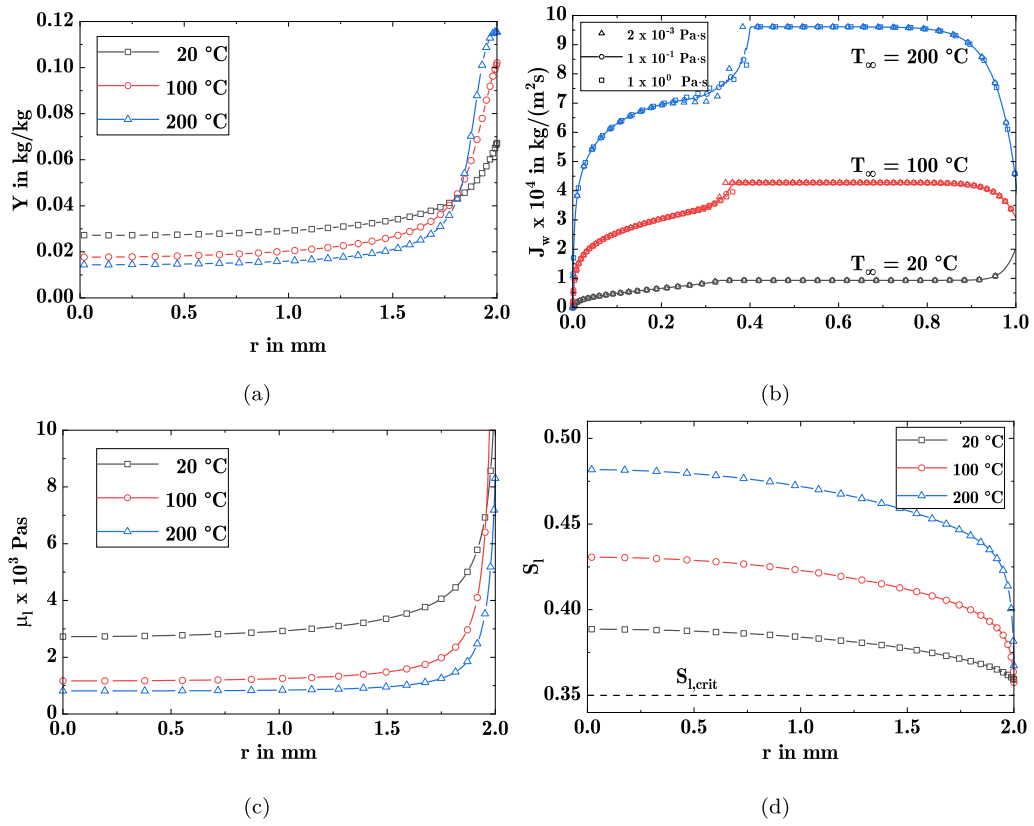

Fig. 8. Results for the drying at varying T_∞: (a) post drying precipitate load distribution and (b) vapor flux across the external surface over saturation, as well as profiles at $S_{surf} = S_{l,crit}$ of (c) μ_l and (d) saturation; all simulations were computed with $\mu_{sat} = 1$ Pa · s and $\sigma_{eff,I} = 0.072$ N/m, if not indicated otherwise.

temperatures, visible in Fig. 8b. This hints towards a slight change in the drying behavior, which is further supported by the observed difference in saturation profiles when the surface saturation S_{surf} reaches $S_{l,crit}$ in Fig. 8d. Clearly, at higher temperature, a significant amount of liquid is still available for convective flow by capillary suction when the falling drying rate period is entered, permitting increased redistribution during the falling drying rate period.

3.4. Controlling the profile

With exception of the drying at constant liquid viscosity $\mu_{l,I}$, all acquired precipitate profiles showed a distinctive accumulation near the drying surface. However, the above gained insights allow to generate a more complex profile by manipulation of the process parameters, as shown in Fig. 9a. There, a sphere filled with a liquid with the non-linear liquid viscosity (41) with a saturation viscosity of $\mu_{sat} = 1$ Pa · s, an initial concentration of $c_{init} = 0.5 c_{sat}$ and $\sigma_{eff,I} = 0.072$ N/m was dried in two stages. In the first stage, the evaporation flux at the surface was kept low by drying at $T_\infty = 20\,^\circ$C and a relative humidity of $\phi = 90\%$. At the end of the constant drying rate period, when $S_{surf} = S_{l,crit}$, the second stage increases the evaporation flux and significantly by reducing the relative humidity to $\phi = 0\%$ and adapting T_∞.

The purpose of the first stage lies in facilitating evaporation and equilibration of the concentration by diffusion simultaneously, as shown in Fig. 9b. The thus induced increase in concentration controlled liquid viscosity leads to a decrease of the convective fluxes and therefore to a saturation profile with a minimum at the drying surface, while the aqueous species is almost fully at saturation. In order to avoid con-

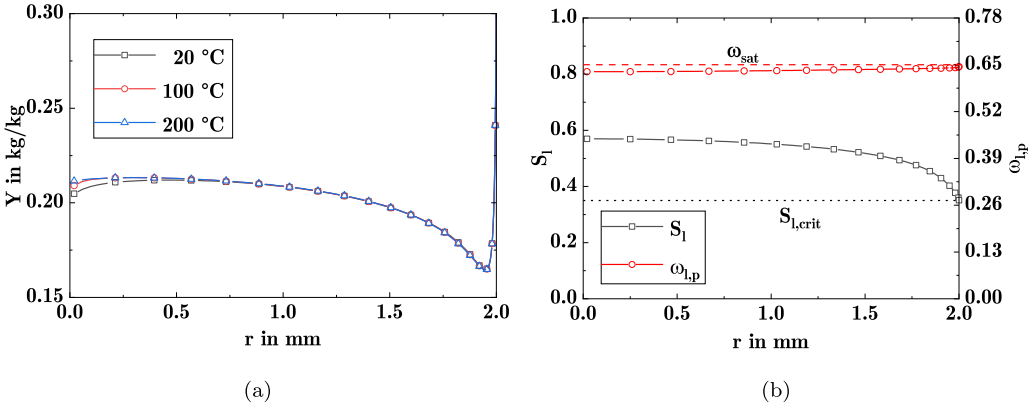

Fig. 9. Results for drying under varying process conditions: (a) post-drying profile with T_∞ during the falling drying rate period and (b) saturation and mass fraction profile at the switch of process conditions.

vective migration to the surface, the drying rate is then significantly increased in the second stage, effectively immobilizing the species in space. However, the convective fluxes are not suppressed totally, allowing some migration towards the surface, leading to a small dip in the center of the sphere, visible in Fig. 9a.

4. Conclusions

Within this investigation, a prior existing averaged drying model has been extended with mass-transport and precipitate formation. This model has then been applied to investigate the drying of heterogeneous catalysts and the impact of viscosity and surface tension couplings with the concentration and temperature fields thereon.

The observations lead to multiple insights: Firstly, the exact form of the coupling of the viscosity with the species and temperature is of high importance to understand the phenomena associated with the drying of porous materials. Whereas the viscosity at saturation is an important indicator for the development of the internal hydrodynamics, alone it does not carry sufficient information to predict the final precipitate distribution.

Secondly, both surface tension force and contact angle have a discernible impact on the hydrodynamics and the precipitate redistribution, however the overall dependency is comparatively low. The reason is, that these parameters stay in the same range of magnitude. In contrast, viscosity is able to change by several order of magnitudes and thus forms a key parameter within this model.

Lastly, the influence of the drying temperature on the overall drying process is not trivial. Its main impact is generated from the increase in vapor flux over the surface, leading to an overall reduction of drying time with higher temperature. Additionally, the increase in local temperature reduces the liquid viscosity, partially counteracting the viscosity change due to higher local concentrations and therefore allows for higher convective fluxes. The thus increased convective fluxes towards the surface lead to less equilibration of species due to diffusion and finally facilitate the formation of more pronounced profiles.

In summary, the addition of a mass-transport model allowed distinguishing the impact of viscosity and surface tension, stressing out the importance of the non-linear coupling of viscosity to the overall dynamics behind preparation of heterogeneous catalysts. The gathered insights have then been applied to define a simple two-stage drying process, demonstrating the possibility to manipulate the precipitate distribution within a porous sphere by solely adapting process parameters. However, it also needs to be emphasized, that transport of precursor species within commonly used porous materials, i.e. silica or alumina, is subject to a variety of additional intricately coupled phenomena. As important examples, diffusion resistance due to viscosity changes or the interplay of ionic species with amphoteric supports should be mentioned (Lekhal et al., 2004). Additionally, the presented model relies on averaged formulations and macroscopic transport coefficients, however heterogeneous catalyst often feature micro- and mesoporous support media, requiring more detailed modeling and better understanding of the pore-level phenomena (Lekhal et al., 2001; Liu et al., 2008; Veldsink et al., 1995; Wu et al., 1998). Further, the presented model does not take into account the Kelvin effect due to the small pore size or the change of local pore morphology due to precipitation and therefore does not incorporate related effects.

In a further step to understand the detailed dynamics behind catalyst preparation and thus improve pre-trial predictions, the proposed model should be extended towards more complex pore size distributions and step-wise increase of the associated transport phenomena. Another interesting direction of research lies in the impact of studying the influence of efflorescence on the drying rate and therefore on the intra-particle hydrodynamics (Gupta et al., 2014), e.g. by extending the capillary model with a population balance. Thus allowing the dedicated study of the impact of the separate phenomena.

Declaration of competing interest

The authors declare that they have no known competing financial interests or personal relationships that could have appeared to influence the work reported in this paper.

Data availability

Data will be made available on request.

Acknowledgements

This work is part of the Advanced Research Center for Chemical Building Blocks, ARC CBBC - 2018.016.C, which is co-founded and co-financed by the Dutch Research Council (NWO) and the Netherlands Ministry of Economic Affairs and Climate Policy. The authors would also like to express their gratitude to Dr.-Ing. Hong Thai Vu for providing them with data for verification.

Appendix A. Validation

A.1. Conservation error

As a means to evaluate the correctness of the finite volume implementation, the conservation error for the moisture content E_X, air E_A, energy E_E and species E_P are continuously computed throughout the simulation process according to (A.1) - (A.4).

$$E_X = \left| \frac{\int_0^R \Delta(\epsilon_l \rho_l \omega_{l,w} + \epsilon_g \rho_g \omega_{g,w})_t \, \mathrm{d}V - \int_{t_0}^t J_w \mathrm{d}t}{\int_0^R \Delta(\epsilon_l \rho_l \omega_{l,w} + \epsilon_g \rho_g \omega_{g,w}) \, \mathrm{d}V} \right| \tag{A.1}$$

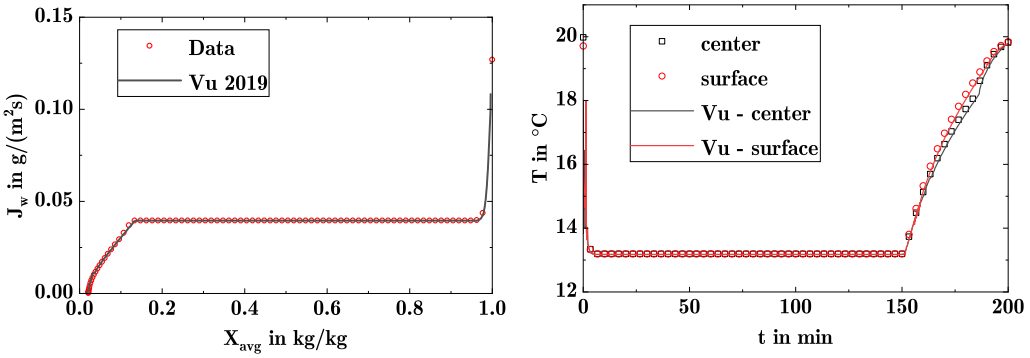

Fig. A.10. Case I: Computed water flux at the surface of the particle with clear constant drying rate and falling drying rate regime a) and temperature at the center and surface of the particle b) compared with (Vu and Tsotsas, 2019).

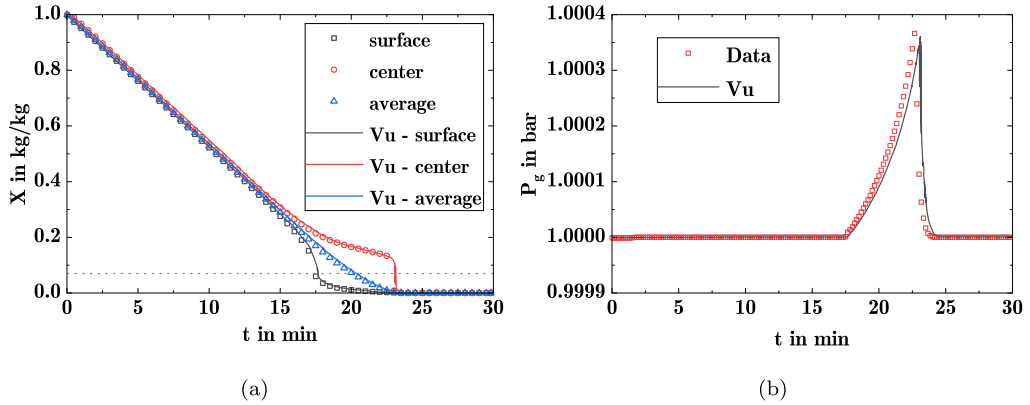

Fig. A.11. Case II: Computed moisture content a) and pressure at the center of the particle b) compared with (Vu and Tsotsas, 2018), the dotted line in a) indicates the moisture content at $S_l = S_{l,crit}$.

$$E_A = \left| \frac{\int_0^R \Delta(\epsilon_g \rho_g \omega_{g,a})_t \mathrm{d}V - \int_{t_0}^t J_a \mathrm{d}t}{\int_0^{R^*} \Delta(\epsilon_g \rho_g \omega_{g,a})_0 \, \mathrm{d}V} \right| \tag{A.2}$$

$$E_E = \left| \frac{\int_0^R \Delta E_t \, \mathrm{d}V - \int_{t_0}^t J_e \mathrm{d}t}{\int_0^R \Delta E_0 \, \mathrm{d}V} \right| \tag{A.3}$$

$$E_P = \left| \frac{\int_0^R \Delta(\epsilon_l \rho_l \omega_{l,n})_t + \Delta(\epsilon_s \rho_s \omega_{s,p})_t \, \mathrm{d}V}{\int_0^R (\epsilon_l \rho_l \omega_{l,n})_0 + (\epsilon_s \rho_s \omega_{s,p})_0 \, \mathrm{d}V} \right| \tag{A.4}$$

Here, the subscript 0 denotes the initial condition of the affected variables. For all simulations E_X, E_A and E_E are well below 10^{-6}, whereas $E_P < 10^{-10}$.

A.2. Drying of light concrete

The implementation of the basic drying model described above has been validated against the available data provided in (Vu and Tsotsas, 2018) and (Vu and Tsotsas, 2019), referred to as case I and II. In both cases, a spherical pellet of light concrete has been simulated. In case I, the drying is conducted at room temperature $T_\infty = 20\,^\circ\mathrm{C}$ with increased humidity $\phi = 0.5$ in the drying air and highlights the temperature and water flux, as seen in Fig. A.10. In contrast, case II focuses on the drying at higher ambient temperature $T_\infty = 80\,^\circ\mathrm{C}$ and the transient profiles of the moisture content and pressure, shown in Fig. A.11. Note, that this validation case does not employ the permeability model described in 2.2 and relies on empirical correlations instead. The associated details can be found in Appendix D.

Both cases show a very good qualitative agreement with the reference data. In Fig. A.11b a slight deviation from the reference data near the end of the drying is visible, indicating a slightly faster occurrence of the drying. However, as the model is quite sensitive towards differences in underlying correlations, implementation and averaging approaches the implementation is considered sufficiently verified.

A.3. Permeability model

The implementation of the permeability model and its derived variables was compared with the results by Vu and Tsotsas (2019). For this verification, a material with a Gaussian pore size distribution of a mean pore diameter of $r_{p,0} = 100$ nm and $\sigma_p = 5$ nm was chosen. The pore size distribution was discretized into 100 bins within 2.5 times of σ_p, $r_{p,min} = 87.5$ nm and $r_{p,max} = 112.5$ nm respectively. Further, $\theta = 0$, $\sigma = 0.0731\ N/\mathrm{m}^2$ and $S_{l,crit} = 0.15$ were employed. Note, that the value of σ and $S_{l,crit}$ are extrapolated from the reported figures and therefore are subject to minor deviations. For the total permeability, $K = 1.237 \cdot 10^{-15}\ \mathrm{m}^2$ was determined, in good agreement with the comparison value of $K_{Vu} = 1.238 \cdot 10^{-15}\ \mathrm{m}^2$, as well as the remaining variables shown in Fig. A.12.

Appendix B. Grid dependency

The grid is subdivided into cells with the width of $\Delta\zeta(\zeta)$, where ζ denotes the dimensionless distance:

$$\zeta = \frac{l}{L} \tag{B.1}$$

with the distance to the no-flux boundary l and the total length of the domain L. The distribution of the cell width is determined by a dedicated function:

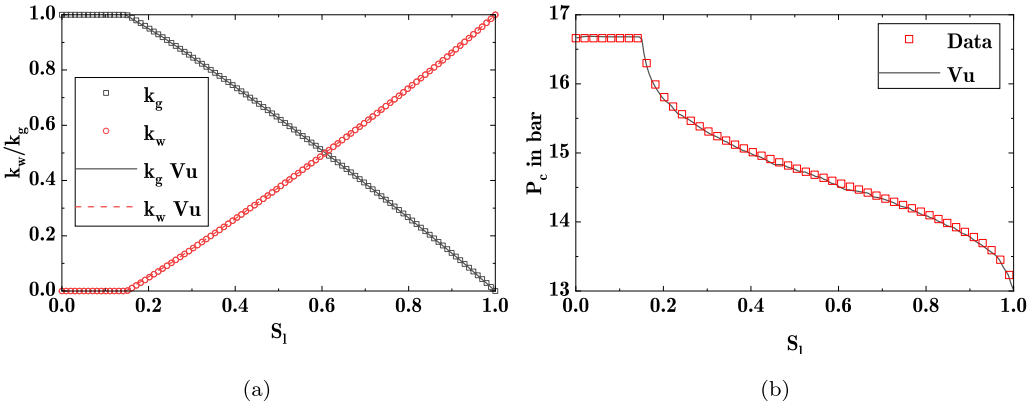

Fig. A.12. Verification of the permeability model and derived variables: partial permeabilities a) and capillary pressure b) with Vu and Tsotsas (2019); the maximum determined deviation was found to be 0.06%.

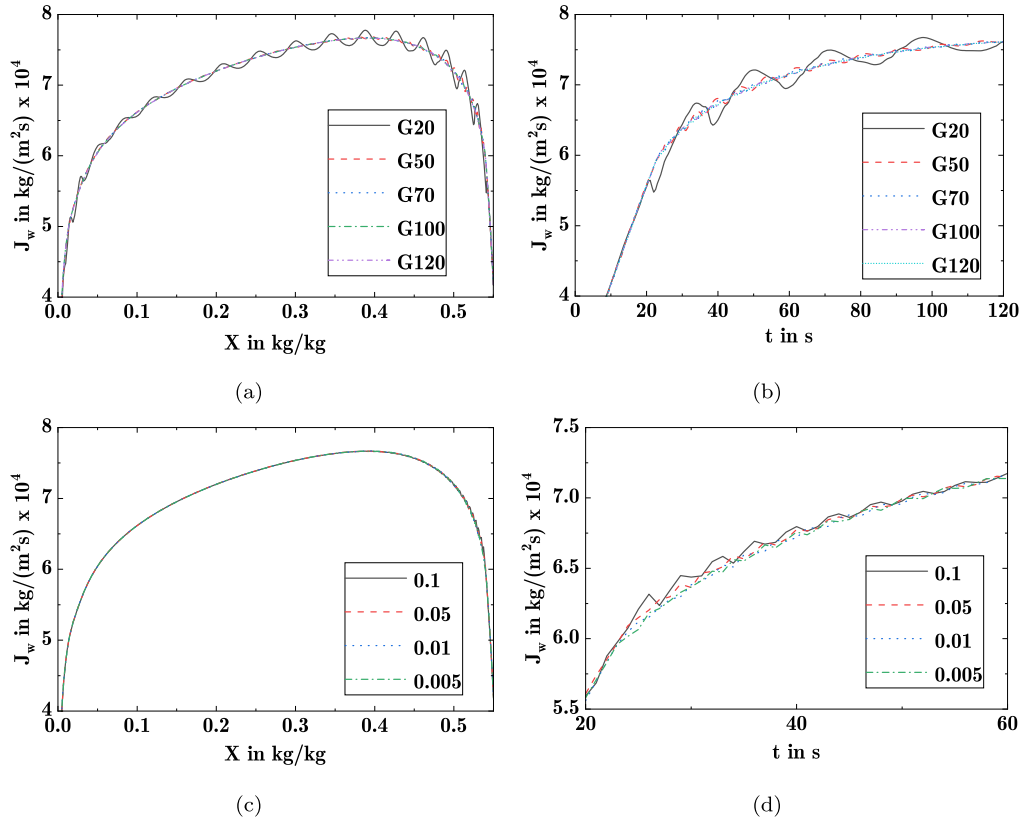

Fig. B.13. Grid dependency for G20-120 cells with $\Delta\zeta_{min} = 0.01$ in (a) and (b), as well as G100 with $\Delta\zeta = 0.005 - 0.1$ in (c) and (d).

$$\zeta = r/R \tag{B.2}$$

$$\Delta\zeta(n) = \frac{(1+\Delta\zeta_{min}) - \zeta(n)}{\sum_n^{n_{tot}}(1+\Delta\zeta_{min}) - \zeta(n)} \tag{B.3}$$

with the grid cell number n and minimal relative grid spacing $\Delta\zeta_{min}$ at $\zeta \longrightarrow 1$. To determine the appropriate grid spacing, the drying of a spherical pellet at $T_\infty = 200\,°C$ with a constant liquid viscosity of $\mu_l = 1\ \mathrm{Pa \cdot s}$ was simulated. As a means to determine the quality of the grid, the water vapor flux J_w at the boundary was chosen due to its dependency on the main transport variables. The results are shown in Fig. B.13. In Fig. B.13a, J_w is displayed in dependency on the average moisture content. There, the introduced oscillations are clearly visible for lower grid resolution, however they do not affect the overall trend of the drying curve. A closer look at J_w during the initial drying is provided in Fig. B.13b. For the current investigation, a grid resolution of 100 grid cells is considered sufficiently accurate.

In a second step, $\Delta\zeta$ was varied and the results are shown in Fig. B.13c and Fig. B.13d. Notably, the overall drying curve in Fig. B.13c does not seem to be affected by the variation of $\Delta\zeta_{min}$. However, inspection of the drying curves in Fig. B.13d reveals the existence of oscillations in J_w. Clearly, with higher resolution towards the surface of the porous pellet, the oscillations are suppressed. For the current investigation, $\Delta\zeta_{min} = 0.01$ is considered sufficient.

Appendix C. Properties and correlations

C.1. Pore size distribution derived parameters

The pore size as shown in Fig. C.14a is generated via (25) with $r_{p,0} = 10$ nm, $\sigma_p = 2$ nm and $C = 0.6$. The permeability of the support

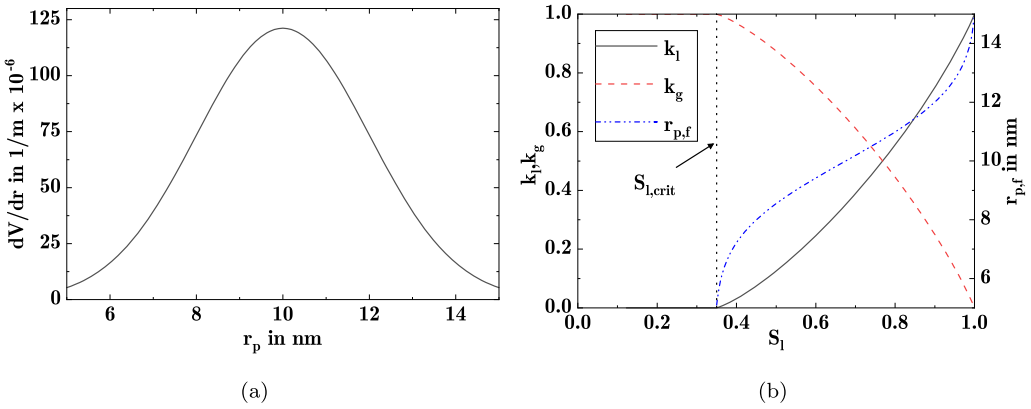

Fig. C.14. Pore size distribution and derived parameters used for the investigation.

Table C.1
Parameters used during the investigation.

Symbol	value	meaning
$\alpha =$	14.25 W/m^2	external heat transfer coefficient
$\beta =$	0.015 m/s	effective mass transfer coefficient
$\epsilon_s =$	0.4	volume fraction of solid
$S_{l,crit} =$	0.35	critical moisture content
$S_{l,init} =$	0.99	initial saturation
$\rho_l =$	1000 kg/m^3	liquid density
$\rho_s =$	2500 kg/m^3	solid density
$\mu_{l,0} =$	0.001 Pa · s	viscosity of pure water
$\mu_g =$	$14.626 \cdot 10^{-6}$ Pa · s	gas viscosity
$M_a =$	29 g/mol	molar weight of air
$M_v =$	18 g/mol	molar weight of water
$M_p =$	130 g/mol	molar weight of transported species
$h_l =$	4190 J/(kgK)$(T - T_{ref})$	enthalpy of the liquid
$h_s =$	960 J/(kgK)$(T - T_{ref})$	enthalpy of the solid
$h_{g,w} =$	1874 J/(kgK)$(T - T_{ref})$	enthalpy of the vapor
$h_{g,a} =$	1006 J/(kgK)$(T - T_{ref})$	enthalpy of the air
$k_{prec} =$	10^4 kg/(m^{3}s)	precipitation reaction rate constant
$\Delta h_v =$	$-2.5 \cdot 10^6$ J/kg	evaporation enthalpy
$\omega_{sat} =$	0.65	saturation weight fraction of aqueous species
$D_{l,wp} =$	$1.67 \cdot 10^{-9}$ m^2/s	effective diffusion coefficient of species
$T_{ref} =$	273.15 K	reference temperature
$P_{ref} =$	101300 Pa	reference pressure

is derived according to (20) and amounts to $K = 7.77 \cdot 10^{-18}$ m^2. In Fig. C.14b, the derived partial permeabilities k_l and k_g according to (21) and (22), as well as the largest filled radius $r_{p,f}$ according to (24) are shown.

C.2. Parameters used for the investigation

An overview over the transport coefficients and auxiliary parameters is provided in Table C.1. The vapor pressure is computed according to the Antoine-equation:

$$P_v = 133.32 \ \exp(18.584 - 3984.2/(T - 39.724)) \text{ Pa} \tag{C.1}$$

For the binary diffusion coefficient of vapor in air, following expression holds:

$$D_{g,av} = 2.26 \cdot 10^{-5} \ (T/T_{ref})^{1.81} P_{ref}/P_g \text{ m}^2/\text{s} \tag{C.2}$$

Note, that here the Kelvin effect is neglected. As shown in Fig. C.15, only in the high viscosity case a minor change in the form of the post-drying precipitation profile. Also, previous works have reached good agreement between model and experimental distributions (Liu et al., 2010). However, further development for validation may require its inclusion.

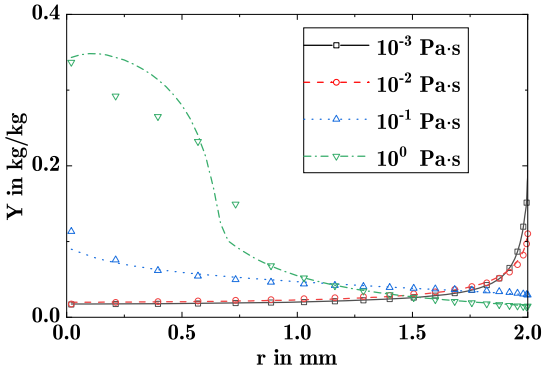

Fig. C.15. Comparison of the impact of the Kelvin effect on the post-drying profiles with constant viscosity values $\mu_{l,I}$ and at $T_\infty = 100$ °C (Lines for results without regarding Kelvin effect, dots for results with Kelvin effect).

Table D.2
Parameters used during the verification.

Symbol	value	meaning
$\epsilon_s =$	0.2	solid volume fraction
$K =$	$2 \cdot 10^{-13}$ m^2	permeability
$k_l =$	S_{fw}^3	liquid side partial permeability
$k_g =$	$1 + (2S_{fw} - 3)S_{fw}^2$	gas side partial permeability
$R =$	2.5 mm	radius of the sphere
$S_{l,init} =$	0.625	initial saturation
$\lambda_l =$	$0.142 + 0.736\epsilon_l/(1 - \epsilon_s)$	thermal conductivity of the liquid
$\omega_{l,p} =$	0	weight fraction of aqueous species

Appendix D. Supplements verification cases

The verification cases described in A.2 are based on (Vu and Tsotsas, 2018) and (Vu and Tsotsas, 2019). If not explicitly mentioned, the same parameters as in Appendix C.2 apply.
In both cases, the drying of light concrete is investigated, once at $T_\infty = 20$ °C and an elevated humidity of $\phi = 50\%$ (case I) and once at $T_\infty = 80$ °C with $\phi = 0\%$ (case II). An overview of the relevant parameters is provided in Table D.2.

For the capillary pressure, following expression was employed:

$$P_c = 40\sigma \exp\left(8.4057 \cdot 10^{-0.5562(S-0.0438)}\right) \text{ Pa} \tag{D.1}$$

With the surface tension:

$$\sigma = -1.3 \cdot 10^{-7}(T - 273.15 \text{ K}) \tag{D.2}$$

$$-1.85 \cdot 10^{-4}(T - 273.15 \text{ K}) + 0.07606 \text{ N/m} \tag{D.3}$$

And μ_l was computed by:

Table D.3
L2 errors for verification case I and II.

T_I	T_{II}	X_{II}	$P_{g,II}$	$J_{w,I}$
0.005 °C	0.17 °C	0.0013 kg/kg	0.2 Pa	0.2 mg/(m² s)

$$\mu_l = -1.27 \cdot 10^{-9}(T - 273.15\ \mathrm{K})^3 + 3.42 \cdot 10^{-7}(T - 273.15\ \mathrm{K})^2 \quad \text{(D.4)}$$

$$- 3.43 \cdot 10^{-5}(T - 273.15\ \mathrm{K}) + 1.56 \cdot 10^{-3}\ \mathrm{Pa \cdot s} \quad \text{(D.5)}$$

The deviation from the reference data is estimated by determination of the L_2-errors according to (D.6). The respective L_2-errors are listed in Table D.3. The conservation errors in (A.1) - (A.4) for two cases do not exceed $5 \cdot 10^{-5}$.

$$L_2(\phi) = \frac{1}{n}\sqrt{\sum_n \left(\phi_n - \phi_{n,ref}\right)^2} \quad \text{(D.6)}$$

where n denotes a data point.

References

Munnik, P., de Jongh, P.E., de Jong, K.P., 2015. Recent developments in the synthesis of supported catalysts. Chem. Rev. 115, 6687–6718. https://doi.org/10.1021/cr500486u. https://pubs.acs.org/doi/10.1021/cr500486u.

Mooiman, M.B., Sole, K.C., Dinham, N., 2016. The precious metals industry. In: Metal Sustainability. John Wiley & Sons, Ltd, Chichester, UK, pp. 361–396. https://onlinelibrary.wiley.com/doi/10.1002/9781119009115.ch16.

Jurtz, N., Kraume, M., Wehinger, G.D., 2019. Advances in fixed-bed reactor modeling using particle-resolved computational fluid dynamics (CFD). Rev. Chem. Eng. 35, 139–190. https://doi.org/10.1515/revce-2017-0059. https://www.degruyter.com/document/doi/10.1515/revce-2017-0059/html.

Maatman, R.W., Prater, C.D., 1957. Adsorption and exclusion in impregnation of porous catalytic supports. Ind. Eng. Chem. 49, 253–257. https://doi.org/10.1021/ie50566a040. https://pubs.acs.org/doi/abs/10.1021/ie50566a040.

Vincent, R.C., Merril, R.P., 1974. Concentration profiles in impregnation of porous catalysts. J. Catal. 35, 206–217. https://doi.org/10.1016/0021-9517(74)90199-7. https://linkinghub.elsevier.com/retrieve/pii/0021951774901997.

Lysova, A.A., Koptyug, I.V., Sagdeev, R.Z., Parmon, V.N., Bergwerff, J.A., Weckhuysen, B.M., 2005. Noninvasive in situ visualization of supported catalyst preparations using multinuclear magnetic resonance imaging. J. Am. Chem. Soc. 127, 11916–11917. https://doi.org/10.1021/ja053456v. https://pubs.acs.org/doi/abs/10.1021/ja053456v.

Bergwerff, J., Lysova, A., Espinosa Alonso, L., Koptyug, I., Weckhuysen, B., 2007. Probing the transport of paramagnetic complexes inside catalyst bodies in a quantitative manner by magnetic resonance imaging. Angew. Chem., Int. Ed. 46, 7224–7227. https://doi.org/10.1002/anie.200701399. https://onlinelibrary.wiley.com/doi/10.1002/anie.200701399.

van de Water, L.G.A., Bezemer, G., Bergwerff, J.A., Versluijshelder, M., Weckhuysen, B.M., de Jong, K.P., 2006. Spatially resolved UV–vis microspectroscopy on the preparation of alumina-supported Co Fischer–Tropsch catalysts: linking activity to Co distribution and speciation. J. Catal. 242, 287–298. https://doi.org/10.1016/j.jcat.2006.06.004. https://linkinghub.elsevier.com/retrieve/pii/S0021951706002028.

Bergwerff, J.A., van de Water, L.G.A., Visser, T., de Peinder, P., Leliveld, B.R.G., de Jong, K.P., Weckhuysen, B.M., 2005. Spatially resolved Raman and UV-visible-NIR spectroscopy on the preparation of supported catalyst bodies: controlling the formation of $H_2PMo_{11}CoO_{40}^{5-}$ inside Al_2O_3 pellets during impregnation. Chemistry 11, 4591–4601. https://doi.org/10.1002/chem.200500116. http://doi.wiley.com/10.1002/chem.200500116.

Liu, X., Khinast, J.G., Glasser, B.J., 2010. Drying of supported catalysts: a comparison of model predictions and experimental measurements of metal profiles. Ind. Eng. Chem. Res. 49, 2649–2657. https://doi.org/10.1021/ie9014606. https://pubs.acs.org/doi/10.1021/ie9014606.

Schlünder, E.-U., 2004. Drying of porous material during the constant and the falling rate period: a critical review of existing hypotheses. Dry. Technol. 22, 1517–1532. https://doi.org/10.1081/DRT-120038738. http://www.tandfonline.com/doi/abs/10.1081/DRT-120038738.

Whitaker, S., 1999. The Method of Volume Averaging. Theory and Applications of Transport in Porous Media, vol. 13. Springer, Netherlands, Dordrecht. http://link.springer.com/10.1007/978-94-017-3389-2.

Vu, H.T., Tsotsas, E., 2018. Mass and heat transport models for analysis of the drying process in porous media: a review and numerical implementation. Int. J. Chem. Eng. 2018, 1–13. https://doi.org/10.1155/2018/9456418. https://www.hindawi.com/journals/ijce/2018/9456418/.

Perré, P., Turner, I.W., 1999. A 3-D version of TransPore: a comprehensive heat and mass transfer computational model for simulating the drying of porous media. Int. J. Heat Mass Transf. 42, 4501–4521. https://doi.org/10.1016/S0017-9310(99)00098-8.

Lekhal, A., Glasser, B.J., Khinast, J.G., 2001. Impact of drying on the catalyst profile in supported impregnation catalysts. Chem. Eng. Sci. 56, 4473–4487. https://doi.org/10.1016/S0009-2509(01)00120-8. https://linkinghub.elsevier.com/retrieve/pii/S0009250901001208.

Noorithaya, A.V., Bishop, C., Sarkar, P., Khinast, J.G., Glasser, B.J., 2019. Drying of supported catalysts for high metal concentrations: a reduced parameter model. Chem. Eng. Sci. 206, 361–374. https://doi.org/10.1016/j.ces.2019.05.014. https://linkinghub.elsevier.com/retrieve/pii/S0009250919304464.

Vu, H.T., Tsotsas, E., 2019. A framework and numerical solution of the drying process in porous media by using a continuous model. Int. J. Chem. Eng. 2019. https://doi.org/10.1155/2019/9043670.

Liu, X., Khinast, J.G., Glasser, B.J., 2008. A parametric investigation of impregnation and drying of supported catalysts. Chem. Eng. Sci. 63, 4517–4530. https://doi.org/10.1016/j.ces.2008.06.013. https://linkinghub.elsevier.com/retrieve/pii/S0009250908003461.

Börnhorst, M., Walzel, P., Rahimi, A., Kharaghani, A., Tsotsas, E., Nestle, N., Besser, A., Kleine Jäger, F., Metzger, T., 2016. Influence of pore structure and impregnation–drying conditions on the solid distribution in porous support materials. Dry. Technol. 34, 1964–1978. https://doi.org/10.1080/07373937.2016.1147048. https://www.tandfonline.com/doi/full/10.1080/07373937.2016.1147048.

Metzger, T., Tsotsas, E., 2005. Influence of pore size distribution on drying kinetics: a simple capillary model. Dry. Technol. 23, 1797–1809. https://doi.org/10.1080/07373930500209830. http://www.tandfonline.com/doi/abs/10.1080/07373930500209830.

Yang, X., Lu, T.J., Kim, T., 2014. An analytical model for permeability of isotropic porous media. Phys. Lett. A 378, 2308–2311. https://doi.org/10.1016/j.physleta.2014.06.002. https://linkinghub.elsevier.com/retrieve/pii/S0375960114005684.

Miao, T., Chen, A., Xu, Y., Cheng, S., Zhang, L., Yan, C., Yu, B., 2021. Permeability models for two-phase flow in fractal porous-fracture media with the transfer of fluids from porous matrix to fracture. Fractals 29, 2150148. https://doi.org/10.1142/S0218348X21501486. https://www.worldscientific.com/doi/abs/10.1142/S0218348X21501486.

Thanh, L.D., Van Nghia, N., Do Van, P., Du Tien, P., Jougnot, D., 2023. A unified model for the permeability, electrical conductivity and streaming potential coupling coefficient in variably saturated fractured media. Geophys. Prospect. 71, 279–291. https://doi.org/10.1111/1365-2478.13295. https://onlinelibrary.wiley.com/doi/10.1111/1365-2478.13295.

Mahiuddin, S., Ismail, K., 1996. Temperature and concentration dependence of the viscocity of aqueous sodium nitrate and sodium thiosulphate electrolytic systems. Fluid Phase Equilib. 123, 231–243. https://doi.org/10.1016/S0378-3812(96)90031-X. https://linkinghub.elsevier.com/retrieve/pii/S037838129690031X.

Abdulagatov, I., Zeinalova, A., Azizov, N., 2006. Viscosity of aqueous Ni(NO3)2 solutions at temperatures from (297 to 475) K and at pressures up to 30 MPa and concentration between (0.050 and 2.246) mol·kg^{-1}. J. Chem. Thermodyn. 38, 179–189. https://doi.org/10.1016/j.jct.2005.04.017. https://linkinghub.elsevier.com/retrieve/pii/S0021961405000972.

Bentaleb, F., Che, M., Dubreuil, A.-C., Thomazeau, C., Marceau, E., 2014. Influence of organic additives on the properties of impregnation solutions and on nickel oxide particle size for Ni/Al_2O_3 catalysts. Catal. Today 235, 250–255. https://doi.org/10.1016/j.cattod.2014.02.020. https://linkinghub.elsevier.com/retrieve/pii/S0920586114001485.

Segur, J.B., Oberstar, H.E., 1951. Viscosity of glycerol and its aqueous solutions. Ind. Eng. Chem. 43, 2117–2120. https://doi.org/10.1021/ie50501a040. https://pubs.acs.org/doi/abs/10.1021/ie50501a040.

Prat, M., Bouleux, F., 1999. Drying of capillary porous media with a stabilized front in two dimensions. Phys. Rev. E 60, 5647–5656. https://doi.org/10.1103/PhysRevE.60.5647. https://link.aps.org/doi/10.1103/PhysRevE.60.5647.

Kharaghani, A., Mahmood, H.T., Wang, Y., Tsotsas, E., 2021. Three-dimensional visualization and modeling of capillary liquid rings observed during drying of dense particle packings. Int. J. Heat Mass Transf. 177, 121505. https://doi.org/10.1016/j.ijheatmasstransfer.2021.121505. https://linkinghub.elsevier.com/retrieve/pii/S0017931021006086.

Dutcher, C.S., Wexler, A.S., Clegg, S.L., 2010. Surface tensions of inorganic multicomponent aqueous electrolyte solutions and melts. J. Phys. Chem. A 114, 12216–12230. https://doi.org/10.1021/jp105191z. https://pubs.acs.org/doi/10.1021/jp105191z.

Lekhal, A., Glasser, B.J., Khinast, J.G., 2004. Influence of pH and ionic strength on the metal profile of impregnation catalysts. Chem. Eng. Sci. 59, 1063–1077. https://doi.org/10.1016/J.CES.2003.12.009.

Veldsink, J., van Damme, R., Versteeg, G., van Swaaij, W., 1995. The use of the dusty-gas model for the description of mass transport with chemical reaction in porous media. Chem. Eng. Journal, Biochem. Eng. J. 57, 115–125. https://doi.org/10.1016/0923-0467(94)02929-6. https://linkinghub.elsevier.com/retrieve/pii/0923046794029296.

Wu, Y.-S., Pruess, K., Persoff, P., 1998. Gas flow in porous media with Klinkenberg effects. Transp. Porous Media 32, 117–137. https://doi.org/10.1023/A:1006535211684.

Gupta, S., Huinink, H.P., Prat, M., Pel, L., Kopinga, K., 2014. Paradoxical drying of a fired-clay brick due to salt crystallization. Chem. Eng. Sci. 109, 204–211. https://doi.org/10.1016/J.CES.2014.01.023.